JOURNAL OF MATERIALS SCIENCE 35 (2000) 5389–5400

Effect of rare-earth oxide(CeO_2) on the microstructures in laser melted layer

Y. M. ZHANG
The Graduate School of Natural Science and Technology, Okayama University, 3-1-1 Tsushima-naka, Okayama 700-8530, Japan; Department of Mechanical Engineering, Okayama University of Science, 1-1 Ridai-Cho, Okayama 700-0081, Japan; Luoyang Institute of Technology, Luoyang 471039, People's Republic of China
E-mail: zhang@mater.mech.okayama-u.ac.jp

M. HIDA
The Graduate School of Natural Science and Technology, Okayama University, 3-1-1 Tsushima-naka, Okayama 700-8530, Japan

H. HASHIMOTO, Z. P. LUO
Department of Mechanical Engineering, Okayama University of Science, 1-1 Ridai-Cho, Okayama 700-0081, Japan

S. X. WANG
Luoyang Institute of Technology, Luoyang 471039, People's Republic of China

The effect of rare-earth oxide (CeO_2) on the microstructures in laser melted layer has been studied via X-ray diffraction analysis and transmission electron microscopy techniques. It is shown that in the laser melted layer, the primary crystallization γ -(Fe,Ni) phase is changed from 3.0 μm to 1.5 μm in average size after the addition of rare-earth oxide; while in the eutectic structure, granular $CeNi_8Si_5$ phase is identified in the CeO_2-addition sample except for the primary crystallization γ -(Fe,Ni) phase and laminar Fe_3B phase which appear in the CeO_2-free sample. Electron microscopical evidences show that quantities of W-rich phases with the molecular formula of $(Cr,W)_7C_3$, are found in the CeO_2-addition sample, it is of orthorhombic structure with lattice parameters of $a = 0.494$ nm, $b = 0.732$ nm, $c = 1.355$ nm. © *2000 Kluwer Academic Publishers*

1. Introduction

The laser surface melting method is one of the techniques available that may improve the surface properties of the alloys while keeping their bulk properties intact [1–5]. By using a high-power laser beam, a thin surface layer of metals and alloys can be melted. Since the melting occurs rapidly and only at the surface, the bulk of material remains cool, thus serving as an infinite heat sink. As large temperature gradients exist across the boundary between the melted surface region and the underlying solid substrate, which results in rapid self-quenching and the solidification. The structures can be of fine-grained nature because of the rapid quench from the liquid phase. The types of microstructures observed include super-saturated solutions, metastable crystalline phase and metallic glasses [6]. Due to laser rapid melting and solidification, the microstructures and the properties of laser melted layer may be improved substantially. Many investigators have studied the microstructures and the properties of laser melted layer of various kinds of metals and alloys [7–14].

The rare earth (RE) elements are widely and successfully used in varieties of area, such as superconducting materials, fluorescent materials, permanent magnet alloys since their incipient application to steels in 1950 [15]. The rare earth elements can make effects on the solidification process and microstructures, decrease the alloy melting points, and always form rich compound in eutectic structures [15, 16]. At present, preliminary applications of rare-earth elements have been used on the improvements of surface, in these applications, most works are on the properties of alloys [17], few study of microstructures is reported in the improvements of surface.

In this paper, we study the effect of RE oxide on the microstructures in laser melted layer by transmission electron microscopy (TEM) and X-ray diffraction (XRD) techniques. Such a study will help understanding of the growth mechanism of RE phase formed in laser rapid melting and solidification.

2. Experimental materials and methods

2.1. Experimental materials

The self-melting alloy powder NiCrBSi with grid of #300 was used in this experiment, its alloy composition is: Cr17, B4, Si4, Fe12, C1.0, and Ni balance (in wt%). Additional WC (20 wt%) powder was added to

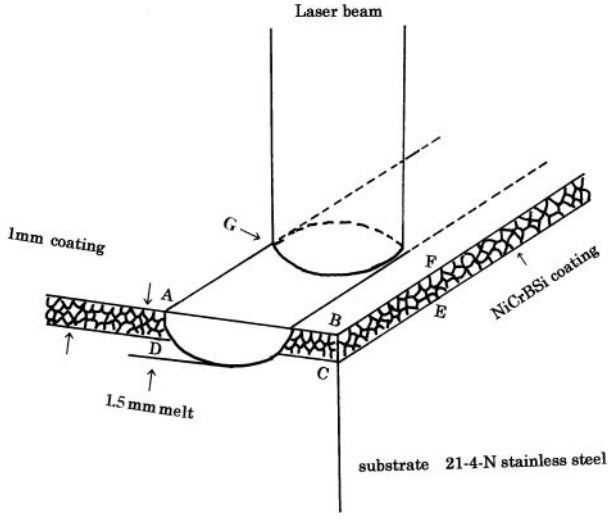

Figure 1 Schematic diagram of laser beam scanning across a solid surface, showing the geometry of the experiments.

the NiCrBSi powder. A high purity CeO_2 (4 wt%) powder was also added to some samples. The matrix was 21-4-N stainless steel, its alloy composition is: Si < 0.25, Mn10, Cr21, N0.4, Ni4, C0.5, and Fe balance (in wt%). The two kinds of mixed alloy powders are used in the experiment as follows:

No. 1: NiCrBSi + 20 wt%WC
No. 2: NiCrBSi + 20 wt%WC + 4 wt% CeO_2

2.2. Experimental methods

The above powders were mixed with 0.05 wt% rosin in a mortar, and grinded with some amount of alcohol, then this mixture was overlayed on the surface of matrix with a size of $8 \times 8 \times 60$ mm^3 (the overlaying depth was 1.0–1.1 mm), then dried it.

The melting of the coating powders was performed by irradiating the HGL-84 Cross-electroexciter CO_2 laser with a power of 2.0 kw as shown in Fig. 1. The working parameters were 2.0 kw, 6.0 mm beam diameter, 7.0 mm/s scanning speed, 250 mm off-focus value, and N_2 gas was used to preserve the melting pool. Slices with 0.3 mm thickness were cut along normal, parallel (along two direction of ABFG and BCEF in Fig. 1) and 45° angle to the laser beam scanning direction, then these slices were thinned mechanically, and ion-milled for TEM samples.

The X-ray diffraction was carried out on a PW 1700 X-ray diffractometer. The energy-dispersive X-ray spectroscopy (EDS) analysis was made on a JEOL JEM 2000FX transmission electron microscopy. TEM observation was carried out using a JEM 4000EX with the resolution of 0.17 nm at 400 kv.

3. Results and discussion

3.1. X-ray diffraction analysis

Fig. 2a and b show the XRD results of (NiCrBSi + WC) and (NiCrBSi + WC + 4wt%CeO_2) coating layers, respectively. From Fig. 2a, five phases are identified. While after the addition of CeO_2 as shown in Fig. 2b, $CeNi_8Si_5$ phase (face-centred cubic lattice, $a = 1.115$ nm) is newly found. Table I indicates the lattice types and parameters of phases in both alloy coating layers. Some peaks with $d = 0.94$ nm, 0.4683 nm, 0.4155 nm, 0.3121 nm and 0.1497 nm in the CeO_2-free sample, and $d = 0.9332$ nm, 0.4666 nm, 0.4142 nm, 0.4031 nm, 0.3114 nm and 0.1699 nm in the CeO_2-addition sample can not be indexed.

3.2. Effect of RE element on the primary crystallization phase

The microstructures in laser melted layer cut along normal, parallel and 45° angle to laser beam scanning direction have been observed by TEM. The primary crystallization phase in the two kinds of samples cut along normal to laser scanning direction are shown in Fig. 3a and b, respectively. Table II lists the EDS results of primary crystallization phase in two kinds of samples. There is a difference between the compositions of two primary crystallization, but electron diffraction experments show that both of the primary crystallization phases are γ –(Fe,Ni) of super-saturated solutions. From the results of EDS analysis of all phases in the CeO_2 addition sample, it is found that there is not RE element in primary crystallization γ –(Fe,Ni) phase,

TABLE II The composition of two primary crystallization phase in the two kinds of samples

Sample \ Element	Si	Cr	Fe	Ni	W
No.1 (wt%)	1.70	6.29	37.60	54.41	0.00
No.2 (wt%)	4.86	4.00	27.27	63.33	0.56

TABLE I Lattice types and parameters in the two kinds of samples

Phase	NiCrBSi + WC	NiCrBSi + WC + 4 wt%CeO_2	Type	A, B, C (nm)	α, β, γ
γ -(Fe,Ni)	---	---	FCC	$A = 0.3596$	
Fe_3B		---	Orthorhombic	$A = 0.5428$	
	---			$B = 0.6699$	
				$C = 0.4439$	
$Cr_{16}Fe_6NiC_6$	---	---	FCC	$A = 1.062$	
Ni_4B_3			Rhombohedral	$A = 0.6428$	
	---	---		$B = 0.4879$	$\beta = 103.3$
				$C = 0.7819$	
WC	---		Hexagonal	$A = 0.2906$	
				$B = 0.2837$	
$CeNi_8Si_5$		---	FCC	$A = 1.115$	

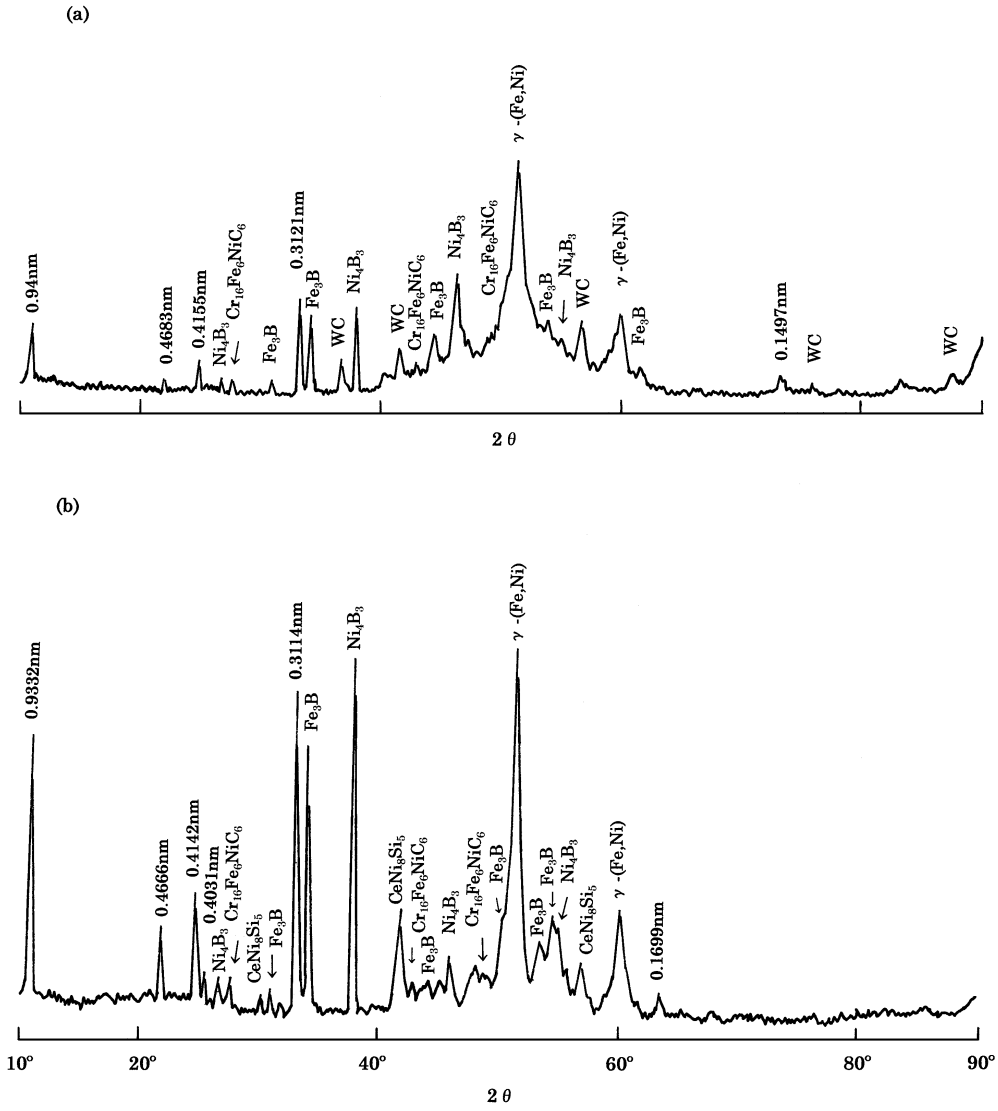

Figure 2 The XRD results in the two kinds of samples (a) (NiCrBSi + WC) coating layer; (b) (NiCrBSi + WC + 4 wt% CeO_2) coating layer.

as shown in Table II, the RE elements only segregate in eutectic structure, this result is in agreement with microdistribution of Cerium in steel AISI 1518 [16].

Fig. 4 shows a series of electron diffraction patterns(EDPs) and their index of γ –(Fe,Ni) phase in two samples. Fig. 4a is the EDP of γ –(Fe,Ni) phase in the CeO_2-free sample, and Fig. 4b–d are the EDPs of γ –(Fe,Ni) phase in the CeO_2 addition sample, from which one can find that some weak spots are showed such as 1, 2 in Fig. 4b, the index of weak spots show compositional modulation structure of γ –(Fe,Ni) phase in the CeO_2-addition sample. By quantitative analysis and observation, it is found that the primary crystallizations in the CeO_2-free sample are mostly dendrite crystals, but in the CeO_2-addition sample the numbers of equiaxed crystal are increased (Fig. 3); and the average size D of γ –(Fe,Ni) phase in the CeO_2-free sample is 3.0 μm, but that in the CeO_2-addition sample is 1.5 μm. Moreover after the addition of CeO_2, the distance between neighbouring primary crystallizations is obviously decreased (Fig. 3b). Thus it is concluded that the CeO_2 addition decreased size D of the primary crystallization phase and distance between neighbouring primary crystallizations.

Because the RE element take part in some reactions and some fine particles are formed, as a kind of non-self nucleation site, such fine particles increase the nucleation rate and block the growth of crystals. In addition, the equilibrium distribution parameter $k_0 = C_s/C_L$ of rare-earth is very small, thus the RE elements are throughly dissoluble in the liquid while in the solid they are dissolved very limitedly [16]. In the process of solidification, the RE elements are enriched in the front of the liquid, such RE elements thus decrease the melting point and break the dendritic crystals (Fig. 3b), the numbers of equiaxed crystal are increased. On the other hand, a little W elements enter into the structure of primary crystallization γ –(Fe,Ni) of super-saturated solutions, and the composition of primary crystallization is modulated (Table II). Therefore, after the addition of RE, the crystal size is decreased and the modulation structure of composition is formed.

3.3. Effect of RE element on eutectic structures

The eutectic structure in CeO_2-free sample is shown in Fig. 5. In the bright field (BF) image of Fig. 5a, it is

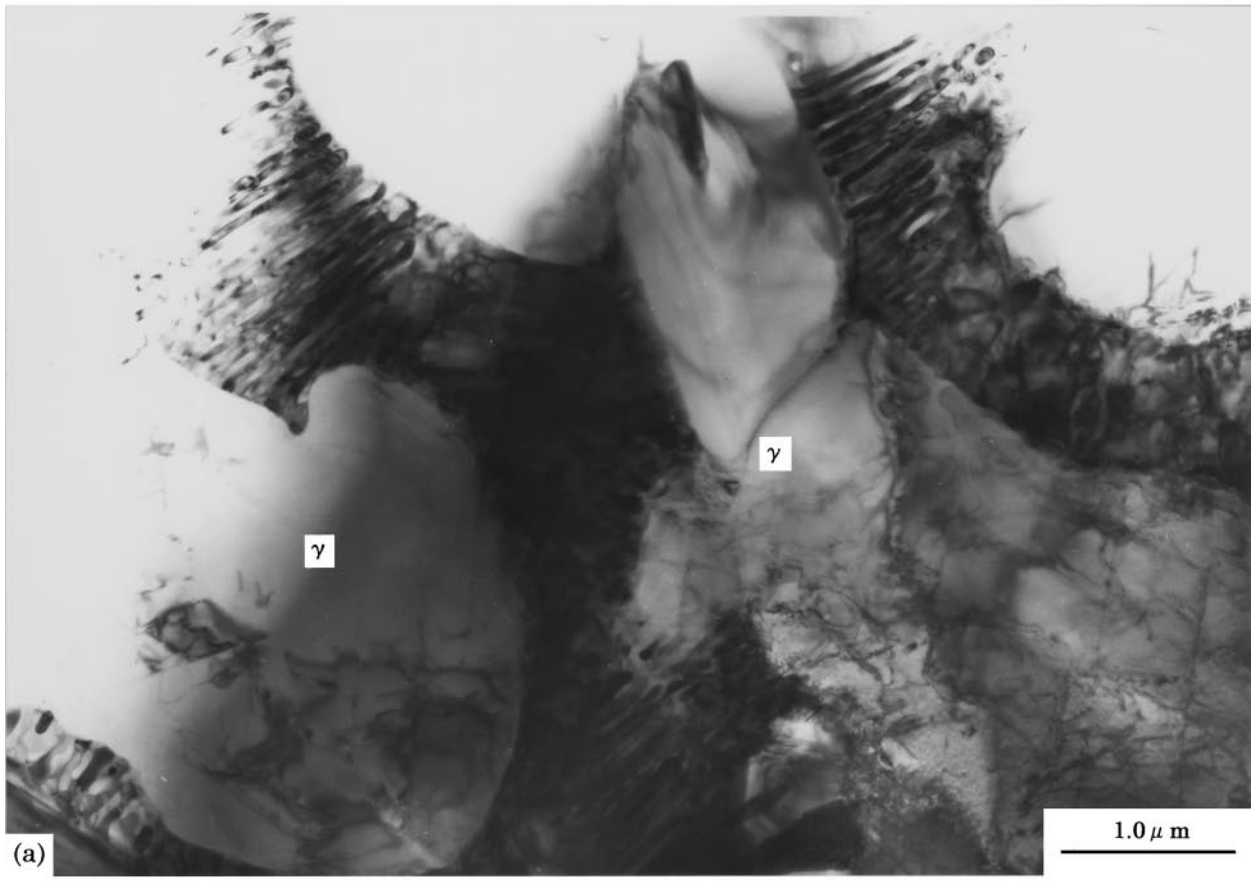

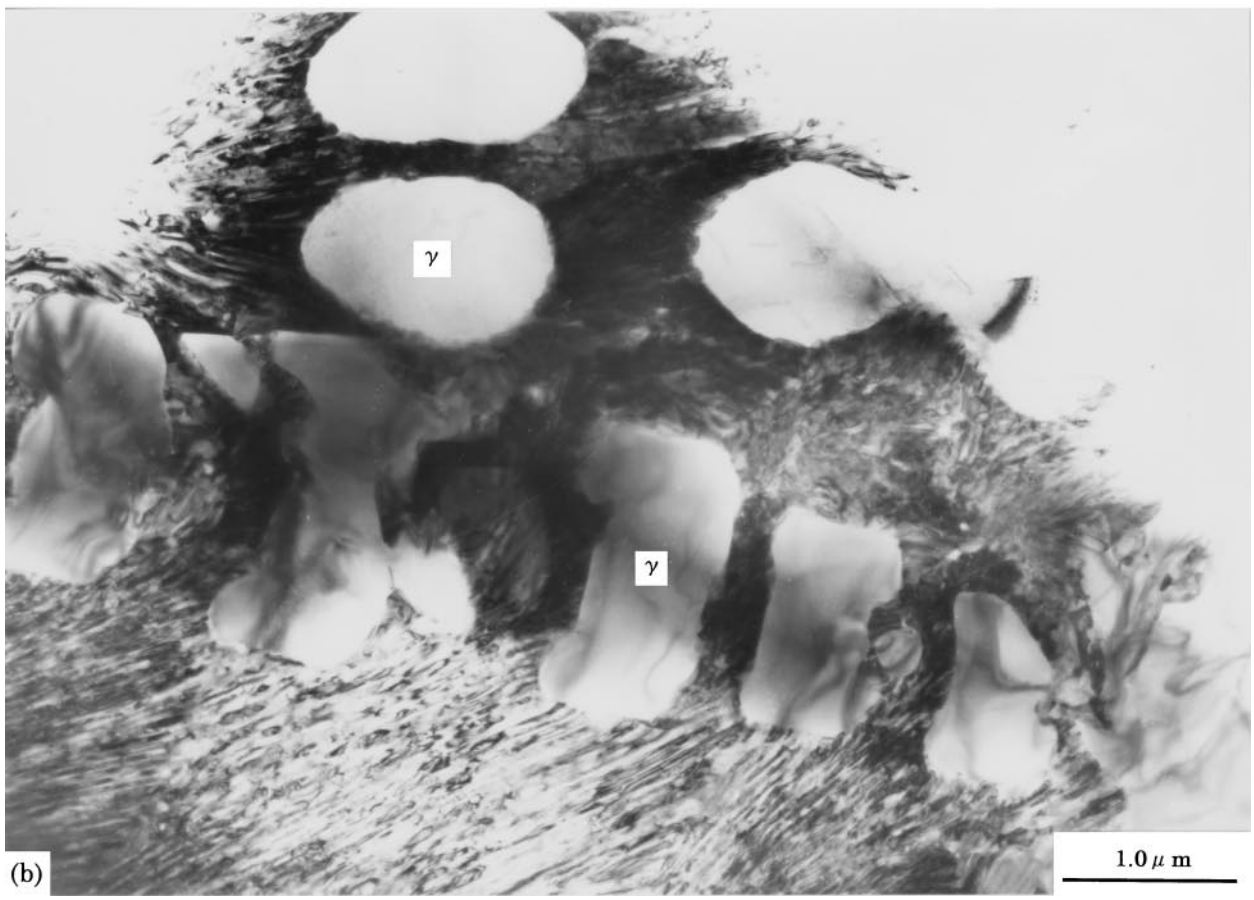

Figure 3 The primary crystallization γ-(Fe,Ni) phase in two kinds of samples cut along normal to laser scanning direction (a) (NiCrBSi + WC) coating layer; (b) (NiCrBSi + WC + 4 wt% CeO_2) coating layer.

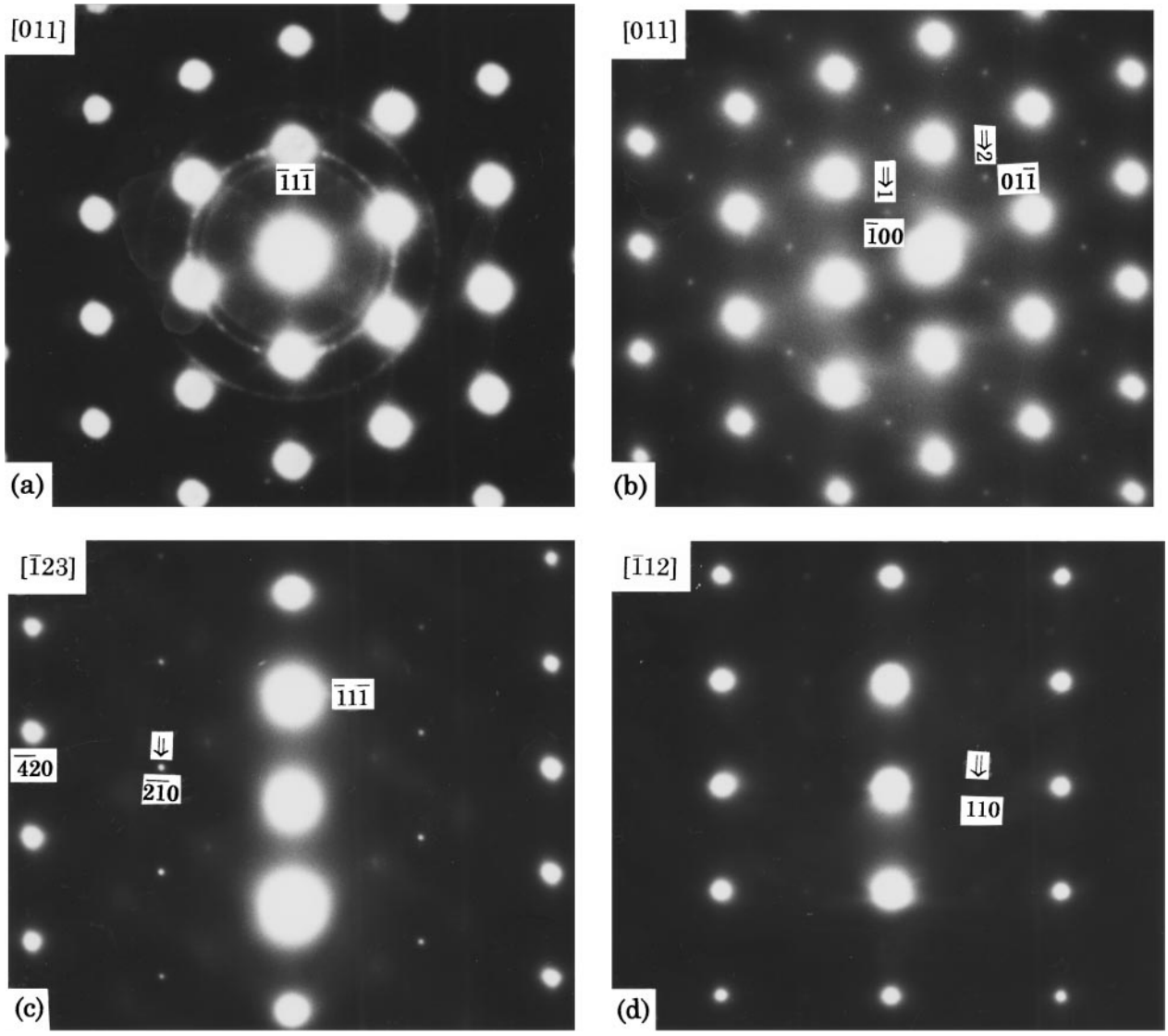

Figure 4 A series of EDPs and their index of γ -(Fe,Ni) phase in two samples (a) (NiCrBSi + WC) sample; (b, c, d) (NiCrBSi + WC + 4 wt% CeO_2) sample.

shown that the eutectic phase is of laminar and rod-type morphology. Fig. 5b shows an enlarged experimental image of the eutectic structure in CeO_2-free sample. Electron diffraction experiments show that the eutectic structure in CeO_2-free sample consists of Fe_3B (A region of Fig. 5b) and γ –(Fe,Ni) (B region of Fig. 5b) phases. The EDP and index including Fe_3B and γ -(Fe,Ni) phase are shown in Fig. 5c. An HREM image projected $[010]_{Fe3B}$ and $[011]_{\gamma\text{-(Fe,Ni)}}$ direction is obtained, as shown in Fig. 6. This HREM image shows that the $\langle 100\rangle_{\gamma\text{-(Fe,Ni)}}$ direction of γ-(Fe,Ni) phase in its (011) plane deviates by 1° from the $[100]_{Fe3B}$ direction. We obtain the lattice corrspondence between the Fe_3B phase and γ-(Fe,Ni) phase as follows:

$$(010)_{Fe3B} \sim \{011\}_{\gamma\text{-(Fe,Ni)}}$$
$$[100]_{Fe3B} \sim \langle 100\rangle_{\gamma\text{-(Fe,Ni)}}$$

After the addition of CeO_2, the eutectic structure is shown in Fig. 7. From the BF image in Fig. 7a, it is found that except for the laminar eutectic Fe_3B phase in the C region which is similar to that in A region of Fig. 5b, another kind of eutectic structure, granular eutectic structure in the D region, is also present. Fig. 7b shows an DF image of the eutectic structure in D region of Fig. 7a. The EDS in Fig. 7c taken from the granular phase shows that such eutectic particles contain Si, Cr, Fe, Ni, and Ce elements. The sizes of these eutectic particles that are measured along two normal directions are 40 nm and 70 nm averagely. By tilting the specimen with large angles, three ED patterns of a particle are obtained, as shown in Fig. 8a. The particle is of face-centred cubic structure with lattice parameter of $a = 1.115$ nm. Thus this eutectic phase is identified as $CeNi_8Si_5$. The EDP and its index from the γ -(Fe,Ni) phase coexisting with $CeNi_8Si_5$ phase are shown in Fig. 8b. An HREM image projected $[001]_{CeNi8Si5}$ and $[001]_{\gamma\text{-(Fe,Ni)}}$ directions is obtained, as shown in Fig. 8c. In both HREM image and ED pattern of Fig. 8b, it is shown that the $[001]_{CeNi8Si5}$ direction of $CeNi_8Si_5$ phase parallels to the $\langle 001\rangle_{\gamma\text{-(Fe,Ni)}}$ of γ -(Fe,Ni) phase, and $(110)_{CeNi8Si5}$ plane of $CeNi_8Si_5$ phase parallels to $\{010\}_{\gamma\text{-(Fe,Ni)}}$ plane of γ-(Fe,Ni) phase, we also obtain the lattice correspondence between the $CeNi_8Si_5$ and γ -(Fe,Ni) phases as follows:

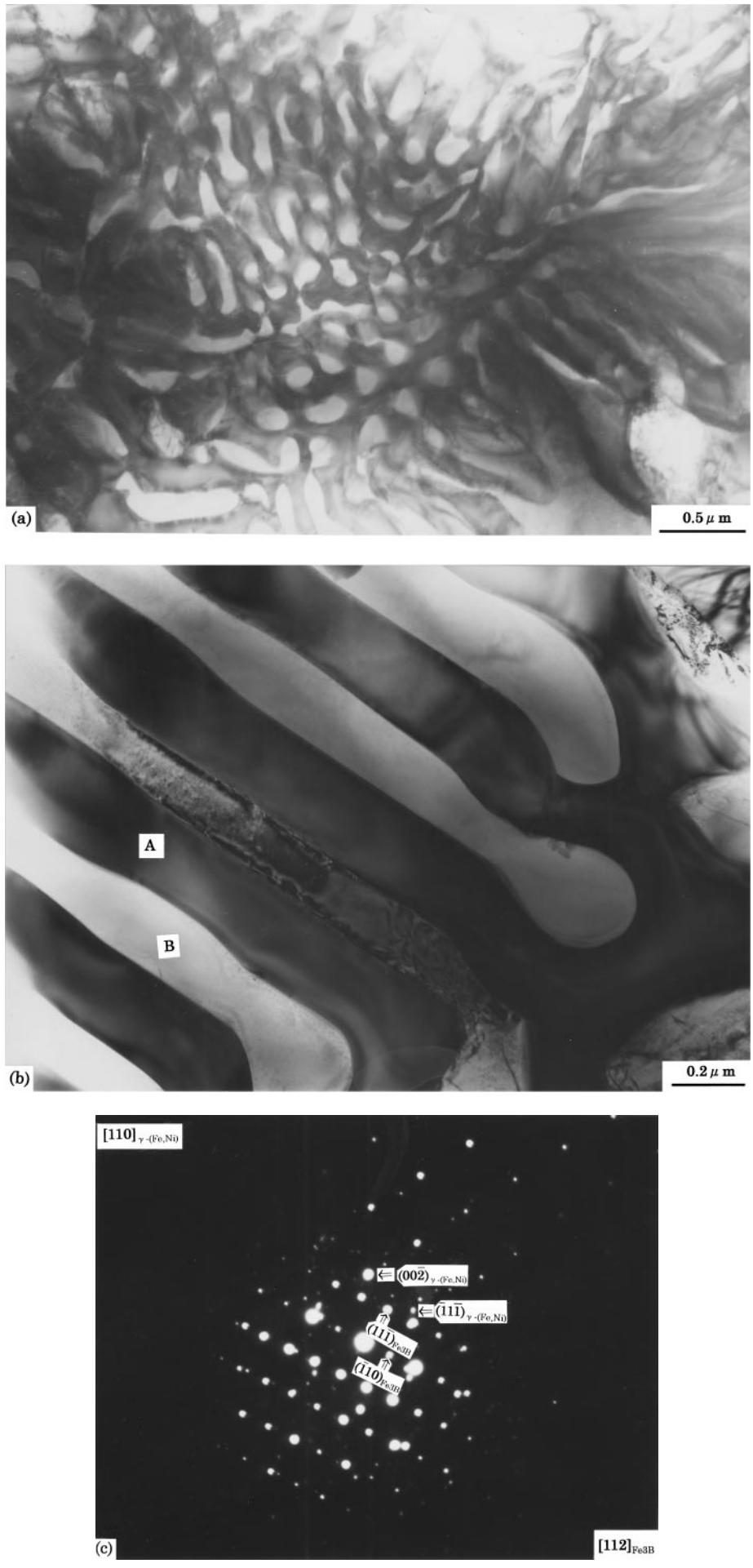

Figure 5 The eutectic structure in CeO_2-free sample (a) the eutectic phase of laminar and rod-type morphology (BF image); (b) an enlarged experimental image of the eutectic structure; (c) EDP and index including Fe_3B and γ -(Fe,Ni) phase.

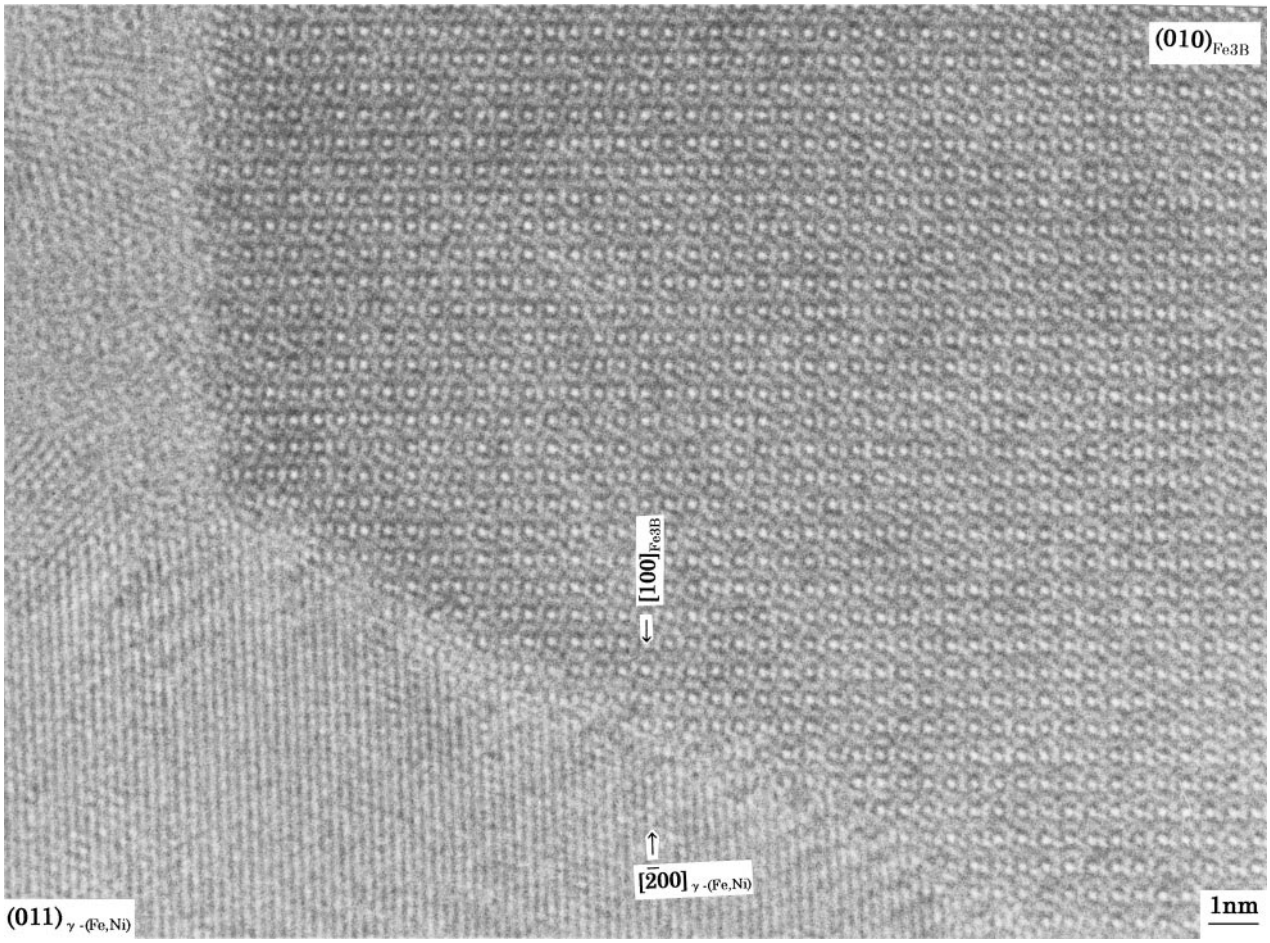

Figure 6 HREM image projected $[010]_{Fe3B}$ and $[011]_{\gamma\text{-(Fe,Ni)}}$ direction in the CeO_2-free sample.

$$(110)_{CeNi8Si5} \sim \{010\}_{\gamma\text{-(Fe,Ni)}}$$
$$[001]_{CeNi8Si5} \sim \langle 001\rangle_{\gamma\text{-(Fe,Ni)}}$$

From the experimental observation, it is seen that the addition of RE element has the effect on changing the eutectic structure. The reason is that the RE element decreases the melting point and prolongs the crystallizing time, also promotes the diffusion of Ni and Si elements in the liquid; meanwhile the RE element with larger atomic size moves quick after separated from constitutive atoms in solid, and diffuses into liquid between dendritic crystals, then the eutectic structure is formed. The granular morphology is formed due to the spheroidizing effect of RE element on eutectic compound [18].

3.4. The promoting decomposition of WC after RE addition

The XRD pattern in Fig. 2a shows that WC phase is present in the CeO_2 –free sample, its morphology is observed using a JSM-35CF scanning electron microscopy (SEM), as shown in Fig. 9. The composition taken from such a phase is: Cr32.95, Fe24.93, Ni14.27, and W27.85 (in wt%), this phase is undissolved WC particle in part.

In laser melting process, WC can not be dissolved wholely due to its higher melting point, therefore it must be also a nucleating site. However, in the sample with 4 wt% CeO_2 added, such WC phase disappeared, while another kind of laminar structure appears in large quantities, as shown in Fig. 10a. The EDS taken from this laminar phase in E region of Fig. 10a is shown in Fig.10b, from which one can find that W element is enriched in laminar phase. A series of EDPs and their index of laminar phase are shown in Fig. 11a. Fig. 11b shows an HREM image of this laminar phase projected [110] direction, this laminar phase is determined as the orthorhombic structure with $a = 0.494$ nm, $b = 0.732$ nm, $c = 1.355$ nm. According to experimental lattice parameters of this phase and their interplanar spacing (d_{hkl}) calculated with above parameters, it is found that some peaks with $d = 0.4666$ nm, 0.4142 nm and 0.4031 nm in Fig. 2b correspond to calculated interplanar spacing (d_{hkl}) of the laminar phase; the same is true of Fig. 2a.

From the result of EDS, it is probable that molecular formula of the laminar phase is $(Cr,W)_7C_3$, and the phase is the same structure as Cr_7C_3 phase. Its structural study is now in progress. In CeO_2 –addition sample, the formation of laminar phase in quantities is due to the effect of RE element which decreases the melting point, thus WC particles mostly are dissociated and the decomposition of WC is promoted in the liquid, then a new compound of rich-W is formed. In addition, in laser melting process, as WC particles in the CeO_2 –free sample is decomposed in part, it is entirely possible that a part of W elements can combine with Cr and C, and $(Cr,W)_7C_3$ phase is also formed.

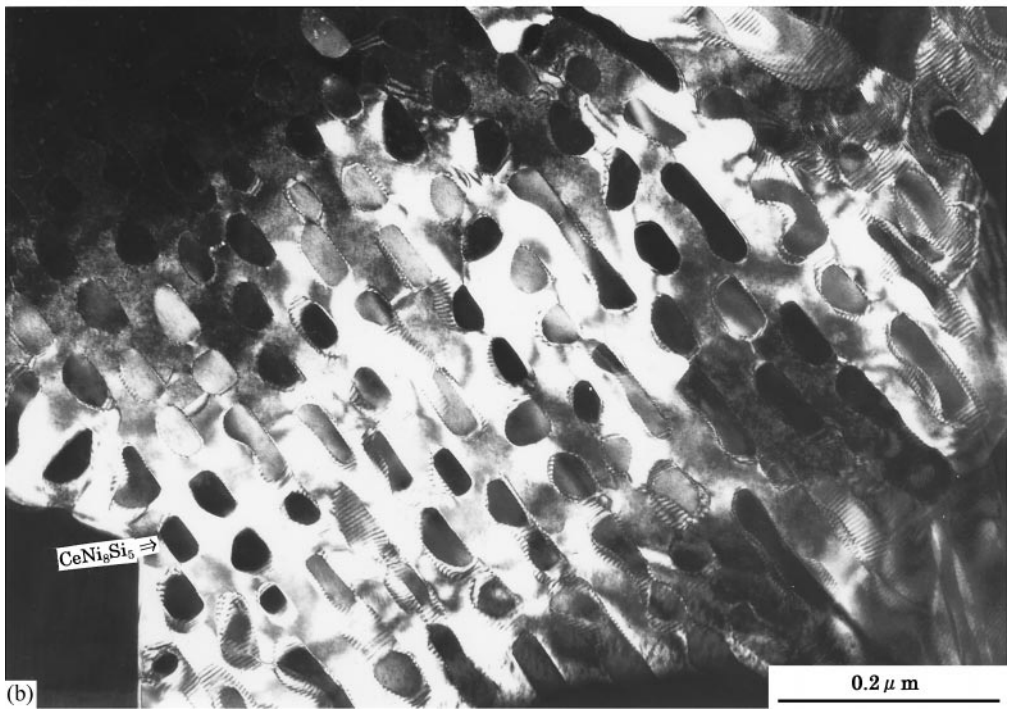

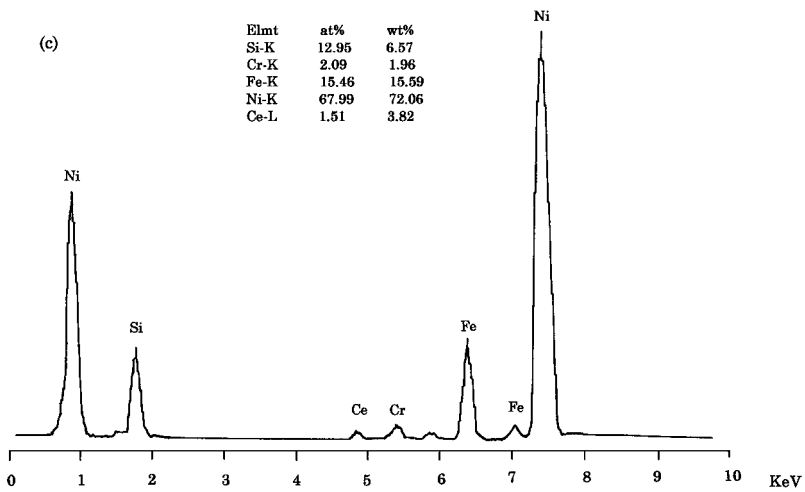

Figure 7 The eutectic structure in the CeO_2 –addition sample (a) the laminar eutectic Fe_3B phase in the C region which is similar as that in A region of Fig. 5b; (b) an DF image of the eutectic structure in D region of Fig. 7a; (c) The EDS analysis on the granular phase.

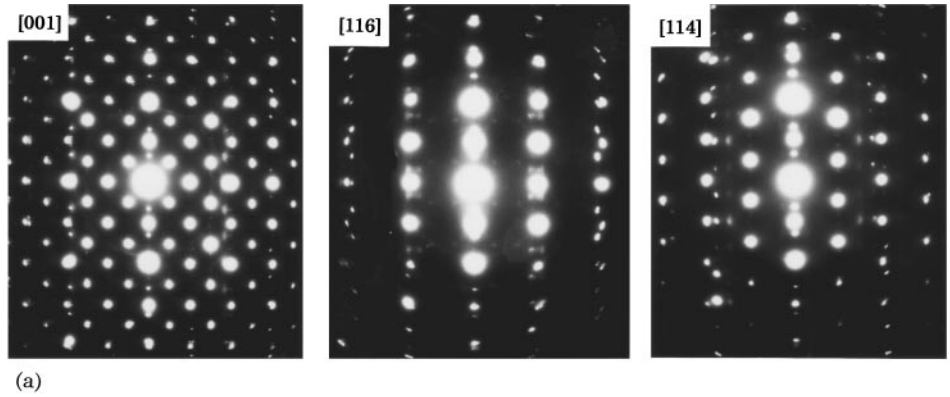

(a)

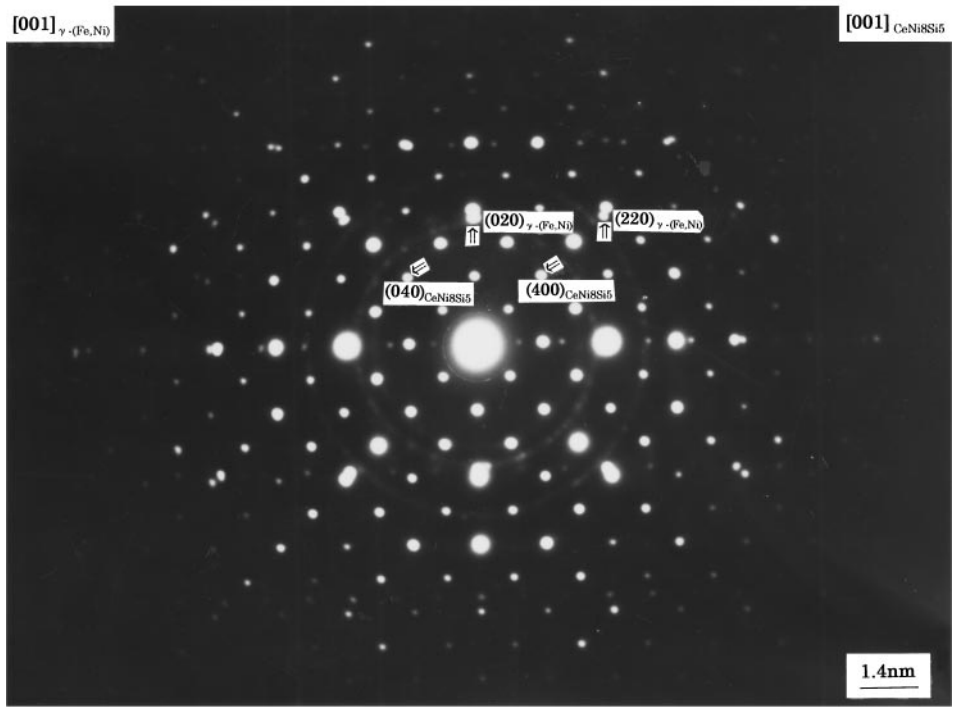

(b)

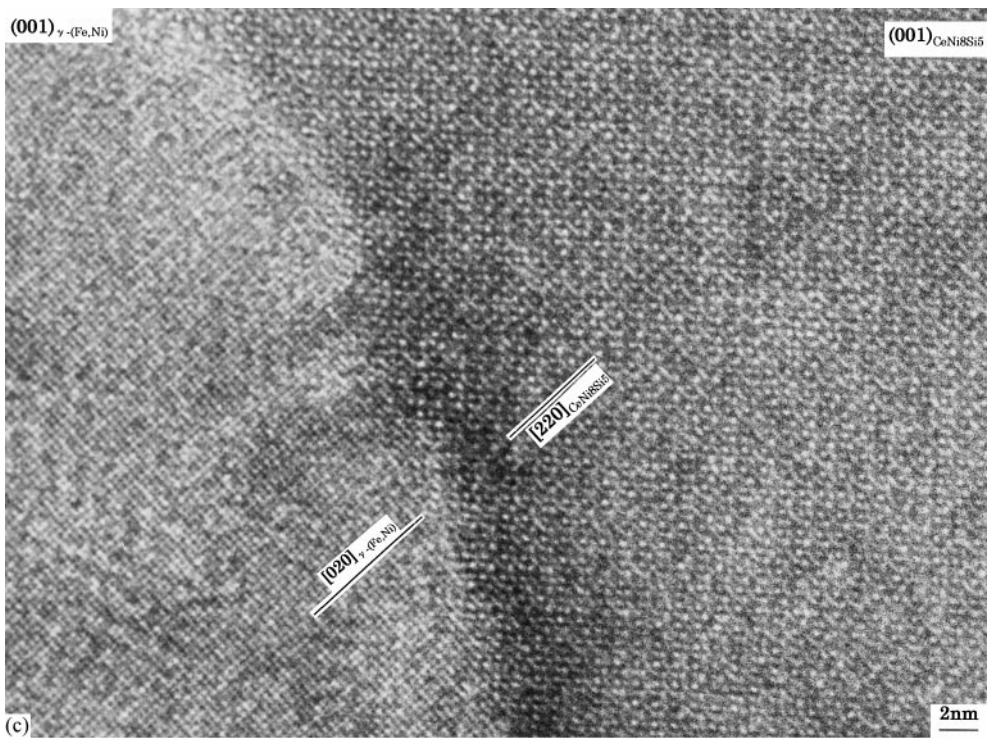

(c)

Figure 8 Rare-earth eutectic phase in the CeO_2 –addition sample (a) the ED patterns of rare-earth phase; (b) the ED pattern and index of including γ -(Fe,Ni) phase and $CeNi_8Si_5$ phase; (c) an HREM image projected $[001]_{CeNi8Si5}$ and $[001]_{\gamma\text{-(Fe,Ni)}}$ direction.

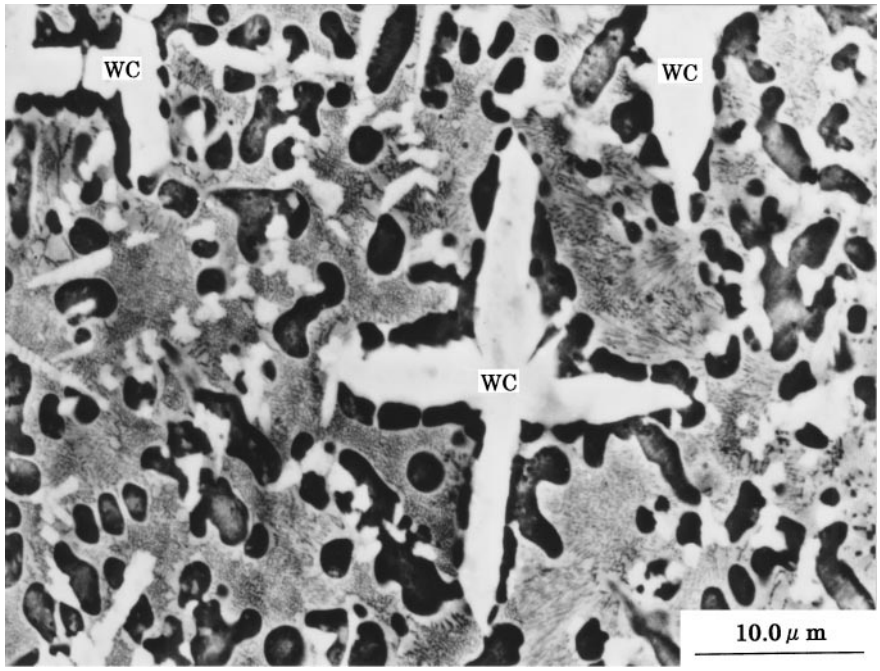

Figure 9 Morphology of WC phase (SEM) in the CeO_2 –free sample.

(a)

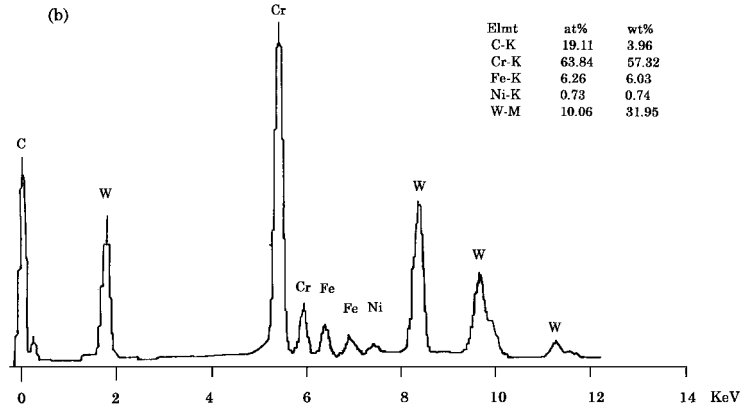

Figure 10 Laminar phase of rich-W in the CeO_2 –addition sample (a) morphology of laminar phase; (b) the EDS analysis of laminar phase.

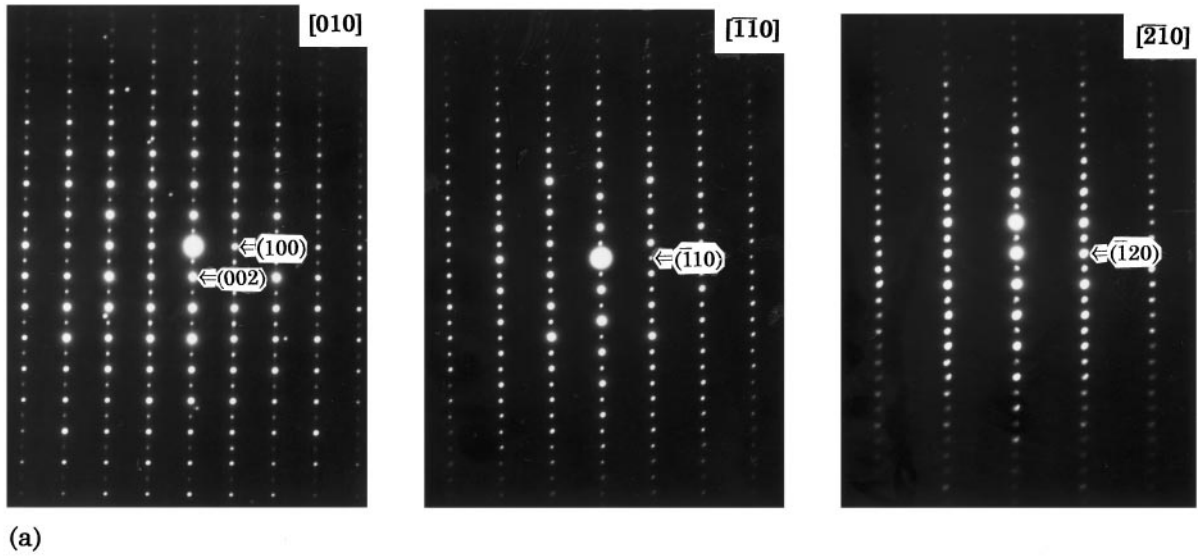

(a)

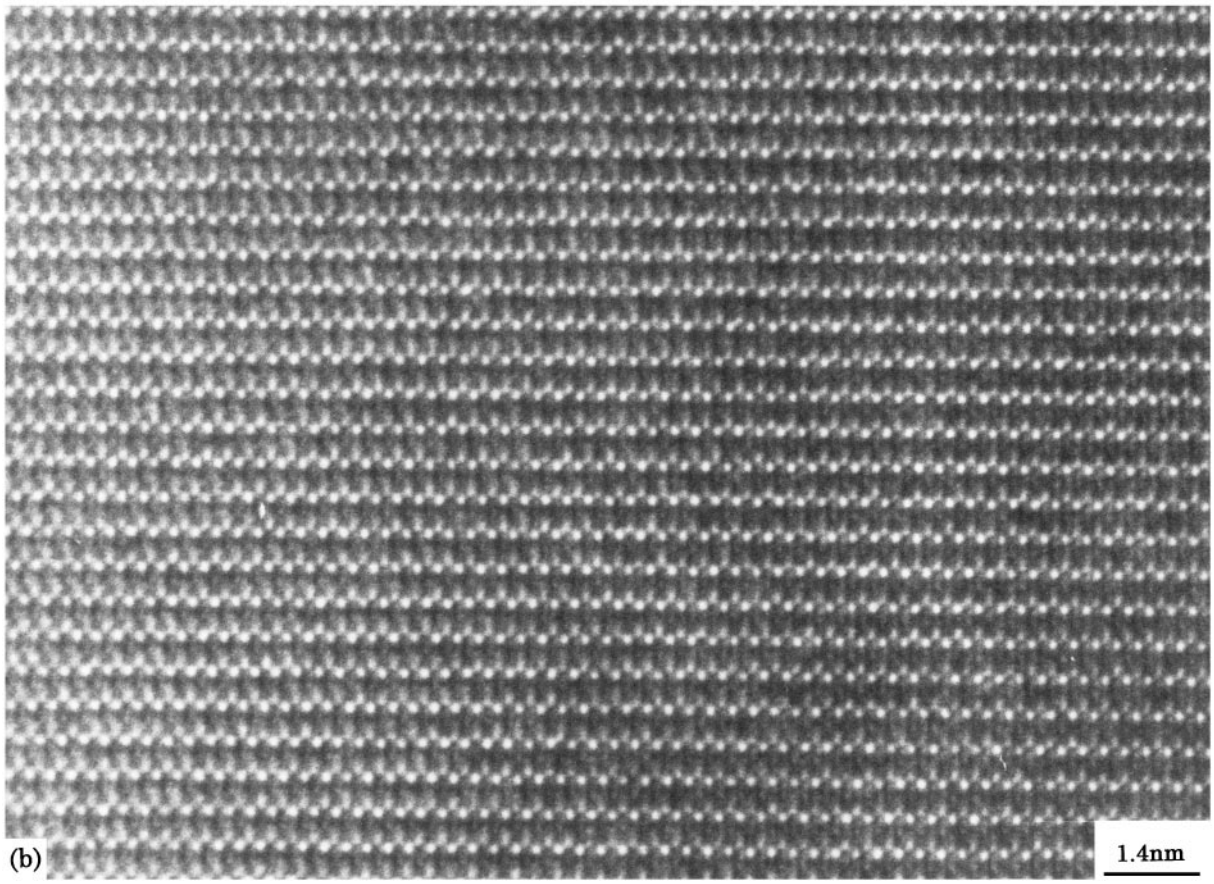

Figure 11 (a) A series of EDPs and their index of rich-W phase; (b) an HREM image of this phase projected [110] direction.

4. Conclusions

4.1 The RE element decreases the size of primary crystallization phase γ -(Fe,Ni) and distance between neighbouring primary crystallization.

4.2 The RE element changes the morphology of eutectic compound, and spheroidizes the eutectic structure;

4.3 The RE element promotes the decomposition of WC phase and quantities of new rich-W phases of $(Cr,W)_7C_3$ are formed. This phase is of orthorhombic structure with lattice parameters of $a = 0.494$ nm, $b = 0.732$ nm, $c = 1.355$ nm.

References

1. P. A. MOLIAN and W. E. WOOD, *J. Mater. Sci.* **18** (1983) 2563.
2. M. F. ASHBY and K. E. EASTERLING, *Acta Metall.* **32** (1984) 1935.
3. U. K. WIIALA, M. S. SULONEN and A. S. KORHONEN, *Surf. Coat. Technol.* **36** (1988) 773.
4. H. DE BEURS, J. A. HOVIUS and J. TH. M. DE HOSSON, *Acta Metall.* **36** (1988) 3123.
5. Y. H. TANG and J. L. DONG, *Wear*. **43** (1991) 145.
6. N. B. DAHOTRE and K. MUKHERJEE, *J. Mater. Sci.* **25** (1990) 445.
7. A. WALKER, H. M. FLOWER and D. R. F. WEST, *ibid.* **20** (1985) 989.

8. JAN KUSINSKI, *Metall. Trans. A.* **19A** (1988) 377.
9. H. J. HEGGE, H. DE BEURS, J. NOORDHUIS and J. TH. M. DE HOSSON, *ibid.* **21A** (1990) 987.
10. D. K. DAS, A. G. PARADKAR and R. S. MISHRA, *Scripata Metall.* **26** (1992) 1211.
11. J. NOORDHUIS and J. TH. M. DE HOSSON, *Acta Metall. Mater.* **41** (1993) 1989.
12. N. ZARUBOVA, P. WOLF, J. CERMAK and M. CERNANSKY, *J. Mater. Sci.* **31** (1996) 137.
13. Q. M. SONG and L. SHEN, *Scripta Mater.* **36** (1997) 531.
14. Y. Y. QIU, A. ALMEIDA and R. VILAR, *J. Mater. Sci.* **33** (1998) 2639.
15. J. F. QIU, "The Application of Rare-Earths to Steels" (Metallurgical Industry Press, Beijing, 1987) p. 330.
16. Q. Y. HAN, C. Z. HUO, W. Z. ZHONG and M. PENG, *Metall. Trans. A.* **18A** (1987) 499.
17. Y. WANG, *Journal of Chinese Rare-Earth.* **10** (1992) 48.
18. W. Z. ZHONG, Q. Y. HAN, C. Z. HUO and X. K. LIU, *Metall. Trans. A.* **18A** (1987) 543.

Received 12 August 1999
and accepted 19 January 2000